https://doi.org/10.5194/egusphere-2026-4668
Preprint. Discussion started: 31 August 2026
© Author(s) 2026. CC BY 4.0 License.

Community Challenge for Image-Derived Observation of Sea Ice Drift and Deformation

Larson Kaidel[1], Christopher Polashenski[1,2]

[1]Dartmouth College Thayer School of Engineering, Hanover, New Hampshire, 03755, United States of America
[2]Cold Regions Research and Engineering Laboratory, Hanover, New Hampshire, 03755, United States of America

Correspondence to: Christopher Polashenski (christopher.m.polashenski@usace.army.mil)

Abstract

Ongoing and unprecedented Arctic sea ice changes impact Arctic life, industry, and the environment. The sea ice cover is becoming younger, thinner, less expansive, and more dynamic; important changes we do not fully understand. Measuring sea ice motion with high fidelity, over large areas and long timescales, is needed to assess how ice dynamics are evolving. Addressing key hypotheses about ice dynamics will improve predictions of Arctic sea ice and climate change and enable developing strategies to adapt to and mitigate adverse effects of sea ice loss. Therefore, we seek to accelerate the development of tools that measure sea ice motion and deformation.

Current tools for extracting sea ice motion from remote sensing imagery produce motion fields too coarse in resolution to resolve individual floes and fractures and have a limited ability to resolve certain types of motion such as floe rotation. Addressing these shortcomings by deploying higher fidelity motion analysis over large areas and at high cadence, is needed to test hypotheses about the effect of small scale fracture mechanics on larger scale motion. We aim to focus such efforts by creating a "community challenge problem" against which methods can be tested. We release a dataset that includes all necessary input imagery and a standardized validation process using ground truth motion derived from extensive drifting buoy networks. The problem is documented in a manner designed to enable contributions to the challenge from outside the core sea ice community.

1. Introduction

Arctic sea ice is increasingly composed of thinner, weaker first-year sea ice (FYI) as multi-year sea ice (MYI) declines (Bi et al., 2020; Liu et al., 2020; Serreze & Stroeve, 2015). Trends of faster ice motion are also observed (Rampal, Weiss, & Marsan, 2009; J. Zhang et al., 2021) and may be connected to the increase in FYI fraction (Itkin et al., 2017; Spreen et al., 2011). Higher deformation rates are observed in FYI, which is typically weaker and thinner than MYI (Maeda et al., 2020; von Albedyll et al., 2021), and an

https://doi.org/10.5194/egusphere-2026-4668
Preprint. Discussion started: 31 August 2026
© Author(s) 2026. CC BY 4.0 License.

increasing frequency of high-deformation winter-time events is predicted as the ice cover type changes (Graham et al., 2019; Rheinlænder et al., 2022a). Many details about these evolving processes, however, remain to be understood or captured in a manner that could be represented in a model. As a result, the net impacts of these changes in the future is uncertain.

Developing new knowledge on the potentially changing dynamics and rheology of sea ice requires observing sea ice motion and accurately and efficiently capturing the displacement, including deformation, of sea ice over large areas and long timescales. Automated extraction of sea ice motion fields from remote sensing imagery and statistical analysis of these fields is the most viable approach for observing sea ice motion over these scales of time and space.

Motion-extracting algorithms process sequential imagery (typically Synthetic Aperture Radar, SAR, images) to retrieve ice motion between images (Curlander et al., 1985). A wide range of such methods are being developed and refined (Fang et al., 2023a; S. Howell et al., 2022; Itkin, 2023; Li et al., 2022; Qu et al., 2024). Some lower resolution methods have been deployed at scale (Kwok, 1996), while many newer methods seek to work with higher resolution imagery. The effort to increase spatial resolution is particularly important. Addressing many questions about the root causes of changes in ice dynamics requires capturing motion at time and space scales that resolve the motion of individual ice floes and can accurately differentiate relative motion and deformation from large scale drift and methodological error.

Unfortunately, development of these newer algorithms has not yet substantially converged toward a widely implemented higher resolution ice motion product. Despite a large number of publications introducing new methods, we are not aware of any recent algorithms that have been applied at basin-wide spatial scale or decadal time scale. The relatively low resolution RADARSAT Geoprocessing System (RGPS) (Kwok, 1996) appears to be the only approach that has been implemented at this 'product' level and available as an observational tool to study changes in sea ice motion (Lindsay et al., 2003; Spreen et al., 2017; Stern & Lindsay, 2009a). There is demand for a higher resolution sea ice motion extracting algorithm that can be used for observing and understanding interannual trends in basin-wide sea ice motion (S. E. L. Howell et al., 2018; Thomas et al., 2011).

The key next steps in making a transition from the many emergent candidate algorithms to a long-term motion product are method error analysis, intercomparison, refinement, and ultimately down selection and implementation at scale. Error analysis and intercomparison currently limit progress. While many candidate algorithms exist, they are not easily compared. Different input images, preprocessing steps, output formats, and accuracy

https://doi.org/10.5194/egusphere-2026-4668
Preprint. Discussion started: 31 August 2026
© Author(s) 2026. CC BY 4.0 License.

assessment methods are used in the publications that introduce them. It is then impossible to directly compare the sea ice motion products without additional preprocessing and assumptions. This difficulty is apparent in the state of the literature. Though most proposed motion analysis methods are accompanied by an accuracy assessment at publication, only a few works directly compare the accuracy of multiple algorithms or methods (Demchev et al., 2017; Girard et al., 2009). This slows convergence toward an automated sea ice motion product that can be used to address many hypotheses about how ice motion is changing. A standard input dataset and validation procedure could mitigate some of these issues, making independent comparisons easier and accelerating progress. The goal of this paper is to suggest one.

One reason convergence has been hard is that markedly improved *accuracy* of sea ice motion observations is needed to understand drift and deformation trends, not just expanded coverage and higher resolution. High accuracy is needed because the most important part of the sea ice motion, deformation, is often a small part of the total motion. Sea ice motion fields can be thought of as including both translational motion (coherent large scale drift) and deformation (relative motion largely caused by fracture and movement of separated pieces of ice). Translational motion is typically much larger, but deformation-driven relative motion represents the actions of mechanisms which break the ice. These mechanisms ultimately constrain the amount of motion possible. Studies on the timing and mechanisms of deformation, such as fracture, ridging (convergence), lead formation (divergence), and shear, therefore, require high-fidelity measurements of motion and high resolutions to resolve the deformation component of the overall motion field accurately (Itkin, 2023; Yu et al., 2009). One challenge is that errors in estimating translational motion (the larger component of the signal) impair observation of deformation. Related and entwined in this challenge is the observation scale-dependence of deformation. At larger scales, multiple opposing internal deformations may cancel (e.g., a lead opening and a ridge formation across a given area), resulting in a lower magnitude of observed cumulative deformation. Finer spatial resolution observations can resolve the multiple deformations, but only if resolved motion is quite accurate (Hutchings et al., 2011), pushing the need for advances in <u>*both*</u> resolution and accuracy. Observations that resolve such deformation help provide insight into deformation scaling (Girard et al., 2009; Hutchings et al., 2011; Marsan et al., 2004; Rampal, Weiss, Marsan, et al., 2009) and the impact of deformation rates or processes on drift speeds and acceleration (Brandt et al., 2022; Feltham, 2008; Kwok, 2002; von Albedyll et al., 2024). If high fidelity and high-resolution sea ice motion maps are routinely available across large areas, hypotheses about the causes of trends in ice motion can be tested. Through these we might understand the observed acceleration of Arctic drift and deformation (Rampal, Weiss, & Marsan, 2009) and its future impact on sea ice extent (Tschudi et al., 2020).

https://doi.org/10.5194/egusphere-2026-4668
Preprint. Discussion started: 31 August 2026
© Author(s) 2026. CC BY 4.0 License.

In an effort to facilitate inter-comparison and stimulate further improvements in sea ice motion analysis methods, we are motivated to provide a "challenge" consisting of curated SAR imagery inputs and data from drifting buoy arrays for validation. We also define a standard validation process using buoy-derived sea ice motion, here in the form of displacement vectors, to eliminate ambiguity in error reporting. The challenge seeks to address shortcomings that we feel constrain development toward an effective motion extracting algorithm. The most apparent constraints are (1) a lack of remote sensing imagery sequences that are paired with contemporaneous, independent, in situ GPS-derived buoy drift paths for validation; (2) a lack of inter-comparison between approaches that could highlight the methods' comparative advantages; and (3) inaccessibility of the problem to non-ice experts particularly in applied mathematics and computer vision. The challenge concept is motivated by other recent papers that present possible algorithms for extracting sea ice motion from remote sensing imagery (Bouillon & Rampal, 2015a; S. Howell et al., 2022; Komarov & Barber, 2014; X. Wang et al., 2023; Yang et al., 2024).

We intend for this challenge to encourage others to evaluate their sea ice motion-extracting algorithms against the standardized and citable dataset and present the defined metrics of performance as one aspect of publications on their methods. Such evaluation is likely to result in a better understanding of each approach's relative strengths and ultimately drive convergence toward optimal approaches.

1.1. Background

Prior efforts to monitor sea ice motion and deformation at large scales focus mostly on automated analysis of repeat Synthetic Aperture Radar (SAR) remote sensing image products. Products from satellite missions such as SeaSat, RADARSAT, and Sentinel-1, which have wide coverage and frequent acquisitions, are most common for this application (Curlander et al., 1985; Kwok, 1996; Muckenhuber et al., 2016). Imagery from these missions vary with temporal (1-10 days) and spatial (10-500m) resolutions spanning several scales (SeaSat, 1978; RADARSAT-1, 1995-2008; Copernicus Sentinel-1, 2014-present).

Development of sea ice motion extraction algorithms began about a decade after satellite remote sensing of sea ice (Fily & Rothrock, 1986). Algorithms have improved as remote sensing image resolution and availability has increased. Early efforts used maximal cross-correlation methods (Fily & Rothrock, 1986; Reddy & Chatterji, 1996). As image processing technology advanced, it has become more common to utilize feature-tracking algorithms, such as scale-invariant feature transform (SIFT) (Lowe, 2004) or speeded-up robust features (SURF) (Bay et al., 2006). Methods perform differently across different ice conditions, however. For example, morphological image processing may better identify and track floes in discontinuous ice fields (Goyal, 2011; X. Wang et al., 2022). Other

https://doi.org/10.5194/egusphere-2026-4668
Preprint. Discussion started: 31 August 2026
© Author(s) 2026. CC BY 4.0 License.

studies are developing approaches that combine methods (A. Korosov et al., 2023) such as cross-correlation (Li et al., 2022), optical flow (SUN, 1996, p. 199), pattern matching (X. Wang et al., 2023), feature tracking (Muckenhuber et al., 2016), and wavelet analysis (Gao et al., 2023). Combining methods may increase the ability of an algorithm to extract motion with a wider range of sea ice conditions (X. Wang et al., 2023).

Contemporary improvements in motion-extracting algorithms are often focused on improving spatial resolution over the RADARSAT Geophysical Processor System (RGPS) (Kwok, 1996). The RGPS is a feature tracking and area matching algorithm, with the capacity to measure motion with rotation. It has been implemented at large time and space scales to generate sea ice motion maps over the Arctic basin spanning 11 years at three-day intervals and 10-25 km spatial resolution (Kwok, 1996; Kwok & Cunningham, 2002). The RGPS has been used to study basin wide sea ice behavior (Ringeisen et al., 2023; Spreen et al., 2017; Stern & Lindsay, 2009b), compare rheologies (Bouchat et al., 2022; Girard et al., 2009), and has been used as a baseline for the development of other sea ice motion-extracting algorithms (Bouillon & Rampal, 2015a; Hutter & Losch, 2020).

Efforts to capture sea ice motion at higher resolutions and accuracy than the RGPS make improvements by changing the intake imagery and developing new image processing tools. The resolution of RGPS was limited by the resolution of the RADARSAT input imagery (100 m) and throughout considerations (Kwok & Cunningham, 2002). Sentinel-1 SAR imagery (40m) is a higher resolution option for input imagery (A. A. Korosov & Rampal, 2017; X. Zhang et al., 2020) that can increase the achievable resolution of extracted motion maps. Improvements in computing capabilities, new image processing techniques, and novel combinations of existing techniques potentially further improve the resolution and accuracy of motion extracting algorithms.

Published algorithms typically present some validation, either using in situ buoy position measurements (Itkin, 2023), manually extracted motion from imagery (Muckenhuber et al., 2016; X. Zhang et al., 2020), or motion fields from other motion extracting algorithms (Thomas et al., 2011) to assess accuracy. Error is commonly reported as a root mean squared error (RMSE) (Demchev et al., 2017; S. Howell et al., 2022; A. A. Korosov & Rampal, 2017). We provide in situ GPS buoy-derived displacement vectors for validation and a standard method for calculating error.

2. Data (methods)

2.1. Case study locations

We curate and present a dataset that includes buoy-derived motion and imagery from two field campaigns: the 2019-2020 Multidisciplinary drifting Observatory for the Study of Arctic Climate (MOSAiC) and the 2021 Sea Ice Dynamics Experiment (SIDEx)

https://doi.org/10.5194/egusphere-2026-4668
Preprint. Discussion started: 31 August 2026
© Author(s) 2026. CC BY 4.0 License.

Beaufort Drift Camp. The MOSAiC campaign, over the central Arctic, and the SIDEx campaign, in the southern Beaufort Sea, capture distinct ice conditions. We select subsets in time that represent diverse ice conditions to test an algorithm's ability to perform under different conditions. Motion-extracting algorithms often perform differently under different ice conditions, with differences in surface conditions (dry/wet) and dynamic conditions (closed pack/opening pack/multiple deformation modes) being most important (S. Howell et al., 2022; Komarov & Barber, 2014; Lindsay et al., 2003).

The MOSAiC expedition (Krumpen et al., 2021; von Albedyll et al., 2021) provides a dense, drifting buoy array capturing ice dynamics over the course over more than a year. MOSAiC operated on two separate areas of sea ice from October 2019 to June 2020 and from June 2020 to October 2020, respectively. We focus on the buoy array that was initially deployed around the first ice floe area. This buoy array captures closed pack ice at high northern latitudes, and major break up, divergence, and export through Fram Strait (Krumpen et al., 2021; Kwok et al., 2004). We select 3 MOSAiC observation periods: the 2-17 January 2020, and 1-20 June to 1-7 July 2020. The period from 2-17 January 2020 represents compact wintertime pack ice, during which the ice camp drifts towards the North Pole in the East Siberian Sea. These observations are bound by 83N to -88N latitude and 90E to -132W longitude. The period from 1-20 June 2020 is characterized by the ice pack approaching Fram Strait and represents spring pack ice with reduced rates of ice regrowth in leads, and a transition to the marginal ice zone. These observations are bound by 80N to -85N latitude and 0E to -20W longitude. The ice has a nearby free edge, and deformation varies in magnitude and mode across 100km scales. This inhomogeneity leads to ice dynamics that are of a different character from the dense wintertime pack ice. The period from 30 June-7 July 2020 is characterized by movement fully into a marginal ice zone, rapid ice disintegration and divergence. These observations are bound by 79N to -82N latitude and 0E to -10W longitude.

https://doi.org/10.5194/egusphere-2026-4668
Preprint. Discussion started: 31 August 2026
© Author(s) 2026. CC BY 4.0 License.

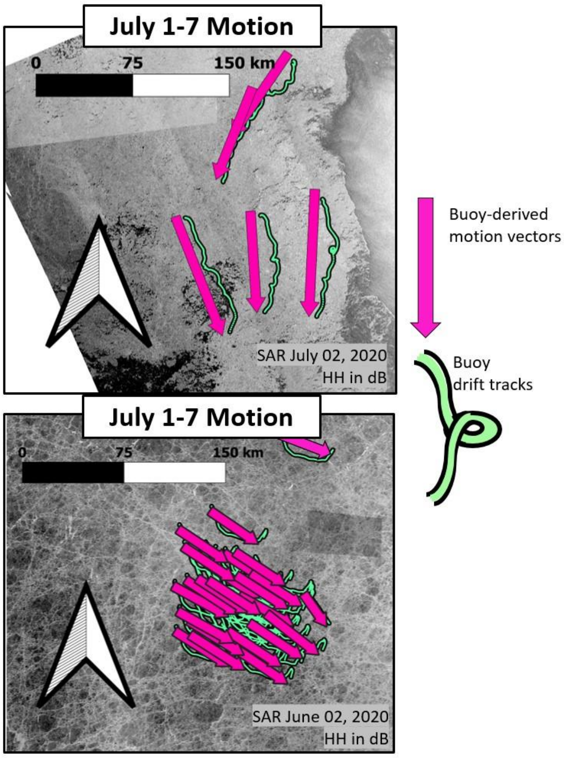

Figure 1. Buoy drift tracks during MOSAiC in the first week of June (a) versus the first week of July (b) in Fram Strait including buoy-derived displacement vectors (c, d)

The Sea Ice Dynamics Experiment (SIDEx) is a smaller drifting camp focused on study of ice dynamics in the Beaufort Sea during late winter and spring 2021. While some buoys reported into September 2021, the majority of observations are taken from March-May 2021 with the buoy array drifting primarily northwestward in the Beaufort Gyre to the Chukchi Sea. This case represents dynamic frozen late winter to spring transition and dynamic conditions including shear along the northern coast of Alaska and acceleration of a closed pack ice throughout the spring (Kwok et al., 2013; Rheinlænder et al., 2022b). Observations from the ice camp between 14 March and 30 May 2021 are bound by 70N to 73N latitude and -150W to -158W longitude. The central floe of the camp is observed to drift a total distance of ~500 km, with average velocities across the array ranging from <1 km/day to 22 km/day (Figure 2).

https://doi.org/10.5194/egusphere-2026-4668
Preprint. Discussion started: 31 August 2026
© Author(s) 2026. CC BY 4.0 License.

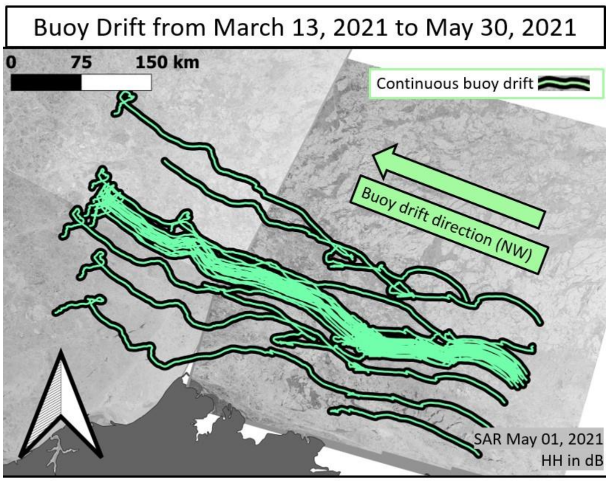

Figure 2. Buoy drift from hourly GPS positions of the SIDEx array from 13 March 2021 to 30 May 2021 with background of Sentinel 1A EW imagery in HH polarization [dB] taken 1 May 2021.

2.2. Buoy-Derived Motion

GPS-derived buoy drift time series serve as validation for algorithm outputs. Processed buoy validation data is presented in a buoy position file that contains position data for each buoy indexed by a unique buoy identification number. The position data includes the initial and final latitude and longitude in WGS84, the latitude/longitude displacement (positive north and east), as well as the vector displacement between the image acquisition times in (m) and direction (clockwise degrees from north). All displacement and bearing calculations are completed using the initial and final latitude and longitude coordinates in radians in a WGS84 ellipsoid projection (Equation 1-Equation 4). We also provide the initial and final latitude and longitude coordinates in EPSG:3413 projection.

$$d = R_e \cdot \varphi \tag{1}$$

Where d is the total displacement in meters, R_e is the radius of the Earth in meters, and φ is the central angle between the initial and final in radians (Royal Institute of Navigation, 1972).

https://doi.org/10.5194/egusphere-2026-4668
Preprint. Discussion started: 31 August 2026
© Author(s) 2026. CC BY 4.0 License.

$$x = \cos(lat_i)\sin(lat_f) - \sin(lat_i)\cos(lat_f)\cos(\Delta lon) \quad (2)$$

$$y = \sin(\Delta lon)\cos(lat_f) \quad (3)$$

$$\theta = \mathrm{atan}\left(\frac{y}{x}\right) \quad (4)$$

Where θ is the angle of direction of buoy displacement from the initial point to the final point in radians and the bearing is degrees clockwise from north, also referred to as initial bearing or forward azimuth.

column label	description	units
ID	buoy identification code	string
lat_i	initial latitude	WGS84 decimal degrees
lon_i	initial longitude	WGS84 decimal degrees
polarlat_i	initial latitude	EPSG:3413 decimal meters
polarlon_i	initial longitude	EPSG:3413 decimal meters
lat_f	final latitude	WGS84 decimal degrees
lon_f	final longitude	WGS84 decimal degrees
polarlat_f	final latitude	EPSG:3413 decimal meters
polarlon_f	final longitude	EPSG:3413 decimal meters
d_lat	change in latitude	WGS84 decimal degrees
d_lon	change in longitude	WGS84 decimal degrees
d_lat_r	change in latitude	WGS84 radians
d_lon_r	change in longitude	WGS84 radians
distance	total displacement distance	meters
y	used to calculate bearing	
x	used to calculate bearing	
theta	angle of buoy bearing not oriented w.r.t. north	radians from east
bearing	bearing of buoy direction	degrees from north

Table 1. Column labels transcribed from the data file and their descriptions and units.

We obtain ice drift data from buoy arrays deployed as a part of the recent field programs MOSAiC and SIDEx, each of which deployed high-density in situ buoy arrays. These present the best available case studies for assessing the accuracy of image derived deformation measurements.[14,41,51] The programs both involve drifting crewed camps on the sea ice, surrounded by dozens (SIDEx) or hundreds (MOSAiC) of drifting buoy systems telemetering Global Positioning System (GPS) position via Iridium satellite. The MOSAiC buoy array comprises a variety of buoys (ASFS, n.d.; “iSVP,” n.d.; Naval Postgraduate School, n.d.; Pacific Gyre, 2024; Perovich & Polashenski, 2024; SAMS Enterprise, n.d.; Y. Wang et al., 2025; Woods Hole Oceanographic Institution, n.d.) using

https://doi.org/10.5194/egusphere-2026-4668
Preprint. Discussion started: 31 August 2026
© Author(s) 2026. CC BY 4.0 License.

a single frequency GPS position with an accuracy of ~3 m reporting every 10 min to 4 hours depending on the buoy type (Bliss et al., 2022). The SIDEx buoy array comprises both single (Pacific Gyre, and SIMB) and dual (SATICE) frequency GPS buoys reporting positions with accuracies of ~3 m or <0.1 m, respectively, with most reporting on intervals between 30 and 60 minutes (Pacific Gyre, 2024; SATICE et al., 2014). Buoy-derived motion includes both large scale drift and relative motion between floes and can capture motion such as rotation and shear. Buoy-derived motion data are interpolated to the Synthetic Aperture Radar (SAR) image acquisition times.

During the MOSAiC expedition a network of GPS buoys operated in varying numbers due to attrition and augmentation deployments. Many types of buoys are featured (Bliss et al., 2022) (Bliss et al., 2023). Array deployments begin in September 2019. Most remaining buoys fail in August 2020 as the ice disintegrated (Bliss et al., 2022). At peak, the buoy network contains 216 buoys and covers an area of approximately 6000 km^2 with spacing from <1 km to ~45 km. During the 1-17 January 2020 period buoys positions are bounded from 84 N to 88 N latitude and 122 E to 103 E longitude, average buoy motion varies from 3 km/day to 14 km/day between image acquisition times. The average divergence or convergence across the array is less than 1.5 m/km per day between image acquisition times. During the 1-20 June 2020 period, buoys are located in Fram Strait between Svalbard and Greenland bounded from 80N to 85N latitude and 0 E to 18 E longitude, drifting approximately 150 km south. Buoy motion ranges from 5.4 km/day to 13.4 km/day increasing as buoys drift south. Average relative motion remains less than 1 m/km per day. From 30 June to 7 July 2020 buoys continue through Fram Strait bounded by 79 N to 82 N latitude and 0 E to 9 E longitude with average motion between 6.6 km/day and 20 km/day. Relative motion increases above 7m/km per day as buoys diverge from an approximately 100 km span to over 500 km (Krumpen et al., 2021). Because of rapid buoy separation during the first week of July, many buoy positions move outside the image boundaries, reducing the number of buoy-derived vectors for the July case.

Over the SIDEx campaign we focus on a period of westward drift bounded by ~71N to ~74N latitude and 145W to 160W longitude between March 13 (42 initial buoys), to May 30, 2021 (10 active buoys). Shear ($\varepsilon_{xy} = 0.23$) along the coast (Figure 3 a-c) is a key feature of the sea ice dynamics in the Beaufort Gyre (Oikkonen et al., 2016). The network comprises up to 30 Pacific Gyre buoys (Pacific Gyre, 2024), 4 SIMB's, and 12 SATICE buoys (SATICE et al., 2014) spaced from 5 to 90 km, covering an approximately 160x90 km area with a dense central buoy area approximately 20x20 km. The center of the buoy array is observed to drift a total distance of about 500 km, with average velocities for each image pair ranging from 0.012 m/s to 0.25 m/s (<1 km/day to 22 km/day). We observe reversals in buoy motion during the period, from 15 km west (April 07-19) to 20 km east (April 19-21), and back to 120 km west (April 21-May 01) (Figure 3 d-f).

https://doi.org/10.5194/egusphere-2026-4668
Preprint. Discussion started: 31 August 2026
© Author(s) 2026. CC BY 4.0 License.

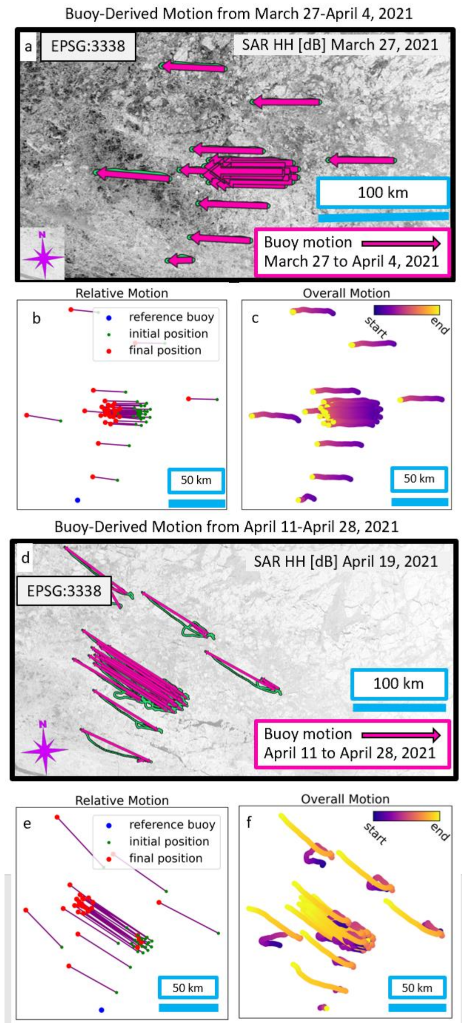

Figure 3. SIDEx buoy-derived motion from the buoy array demonstrating shear along the coast from 27 March to 4 April 2021 (a-c) and 11-28 April 2021 (d-f) example buoy-derived displacement vectors with a background SAR backscatter in HH polarization [dB] image on 27 March 2021 (a) and 19 April 2021 (d), net motion relative to buoy nearest to coast (blue dot) (b and e), and hourly position (c and f).

We determine buoy validation positions at each SAR image acquisition time by linearly interpolating reported buoy positions to the image acquisition time. We exclude buoys that did not report position within 24 hours of the SAR image acquisition time. Most buoy positions are interpolated only over 1 hour or less. We calculate buoy displacement vectors using the change in latitude and longitude to calculate the distance from initial positions and displacement angle from north. We then determine the initial and final buoy positions

https://doi.org/10.5194/egusphere-2026-4668
Preprint. Discussion started: 31 August 2026
© Author(s) 2026. CC BY 4.0 License.

in the projection of the preprocessed SAR images (EPSG:3413). We remove buoys whose initial or final positions are outside the initial or final image boundaries.

2.3. Remote Sensing Imagery

Sentinel-1 SAR imagery from ESA is the most widely used source for active efforts to development automated sea ice image processing algorithms. We provide a standardized dataset of pairs of preprocessed Sentinel-1 SAR images which overlap spatially and temporally with the buoy-derived motion data described above. We conduct preprocessing steps to make the images highly accessible to non-experts. Image sequences are acquired at several different times in the annual cycle, represent multiple ice conditions and behaviors or modes of deformation.

The Sentinel-1 mission provides high resolution all-weather day and night imaging with temporal coverage from April 2014-present (ESA & Copernicus, 2024; Potin et al., 2021). The continually operable satellite of the Sentinel-1 mission (S1A) is outfitted with a C-band synthetic aperture radar (SAR) instrument (5.405 GHz) (Geudtner et al., 2014). Images are captured in four acquisition modes: Interferometric Wide Swath (IW), Extra Wide Swath (EW), StripMap (SM), and Wave (WV) (Potin et al., 2021). In polar areas, the baseline imaging modes are IW and EW which provide a 250 km wide swath and 5x20 m resolution or a 400 km wide swath and 20x40 m resolution respectively (Geudtner et al., 2014). For this project we use exclusively EW mode imagery. Data are captured in HH+HV polarizations (Potin et al., 2021). A single satellite of the constellation (e.g., S1A) acquires repeat images with an identical orbit position every 12 days. Allowing for different viewing geometry, however, revisit periods are less than 3 days in high latitudes (>70N) (Attema et al., 2008; Geudtner et al., 2014) with a north latitude limit at 82N. During a two-satellite constellation mission, either S1A and S1B from 2016-2021 or S1A and S1C from 2026-present (ESA, 2025; ESA & Copernicus, 2024), the temporal resolution can be as low as 1 day (80N-81N) and 2 days (>70N) in EW mode (Castriotta, 2022; Copernicus & ESA, 2022).

The ESA continuously releases level-0 and level-1 Sentinel-1 products. We process level-1 GRD products for this application. (ESA & Copernicus, 2024) L1-GRD products consist of focused L0 raw data, multi-looked and projected using the WGS84 ellipsoid. L1-GRD products are available for all beam modes for all polarizations with resolution classes depending on the level of multi-looking (full, high, or medium resolution) (Riccardo Piantanida, 2022). L1-GRD must be further preprocessed for most applications.

2.4. Image Preprocessing

We further preprocess Sentinel-1 images from the L1-GRD medium resolution product (40x40 m pixels) (Hajduch & Bourbigot, 2021) to standard ready-to-input image pairs

https://doi.org/10.5194/egusphere-2026-4668
Preprint. Discussion started: 31 August 2026
© Author(s) 2026. CC BY 4.0 License.

compatible with the expected motion-extracting algorithms. Here we describe our preprocessing steps (Figure 4).

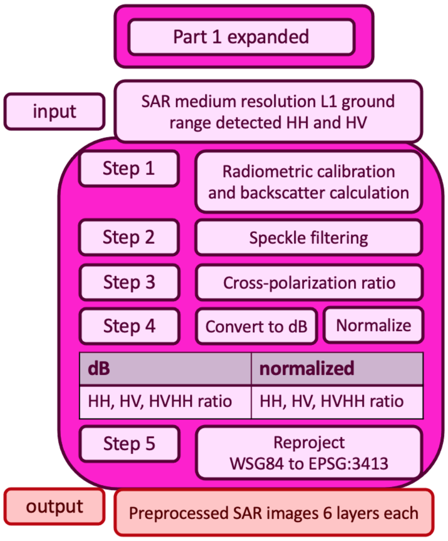

Figure 4. Part 1 of the workflow expanded to steps including basic preprocessing, higher-level correction, and reprojection.

Level-1 ground range detected (L1-GRD) products are downloaded from the Alaska Satellite Facility (ASF) Vertex search portal. These images comprise amplitude and intensity values of each polarization (HH and HV) and look up tables of radar viewing geometry. Pixels in these files are projected onto the ground range with an Earth ellipsoid model (WGS84) resulting in approximately square 40x40m pixels (EarthData & VITO, 2021; Guaragnella & D'Orazio, 2019). L1-GRD products are compatible with the SNAP Sentinel Toolbox, an open-access platform for preprocessing, viewing, and analyzing Sentinel-1 SAR images (ESA, 2024). We use the SNAP toolbox to conduct further preprocessing steps.

First, we radiometrically calibrate the backscatter intensity, using the radar cross-section provided in the look up tables of radar viewing geometry to convert detected reflectivity to σ^0 backscatter, a value of returned radar power normalized over the radar cross-section (Small, 2011). This radiometric calibration should allow imagery from different sensors (e.g. S1A and S1B) or different acquisition times and viewing geometries to be used interchangeably as input into image processing algorithms. (Laur, H., Bally, P., Meadows, P., Sanchez, J., Schaettler, B., Lopinto, E., & Esteban, D., 2002; Liew, 2001; Tan et al., 2018). Each polarization (HH and HV) is calibrated separately, resulting in backscatter coefficients for each polarization at each acquisition time (Part 1 step 1).

https://doi.org/10.5194/egusphere-2026-4668
Preprint. Discussion started: 31 August 2026
© Author(s) 2026. CC BY 4.0 License.

Next, we reduce speckle. All SAR imagery has speckle-type noise. Removing speckle improves the interpretability of the image for identifying trackable features. Numerous methods exist to remove speckle. All have benefits and drawbacks (Lee et al., 1999). We utilize multi-temporal Lee Sigma speckle filtering to reduce speckle without reducing resolution (Lee et al., 2009; S. Quegan et al., 2000). We apply a Lee Sigma filter with 4 looks, a sliding window size of 5x5 pixels, an output window target of 3x3 pixels, and a default sigma value of 0.9 for both HH and HV polarizations (Part 1 step 2).

We calculate the cross-polarization ratio between HH and HV images (Equation 5) (Karvonen, 2014) only after calibration and speckle reduction are completed, as typically recommended (Toyota et al., 2021; Zhou et al., 2018). The additional cross-polarization backscatter coefficient ratio layer may help differentiate features that look similar viewed in HH or HV polarization only (Shokr & Sinha, 2023).

$$R = \frac{\sigma^0_{HV}}{\sigma^0_{HH}} \tag{5}$$

Backscatter does not typically fall into a linear distribution (Qu et al., 2024) so the radar cross-section normalized backscatter coefficient (σ^0) values are all converted to dB with an absolute maximum range from -35 dB to 10 dB, where the majority of images fall within the expected range from -20 dB to 5 dB for sea ice imagery (part 1 step 4). This conversion improves image contrast without altering the features in the image. Subsequently, we normalize the cross-section normalized backscatter coefficient (σ^0) values in each layer of the calibrated and speckle reduced images on a scale from 0-1 (Equation 6) and provide these separately.

$$\boldsymbol{\sigma^0_n = \frac{\sigma^0 - \sigma^0_{min}}{\sigma^0_{max} - \sigma^0_{min}}} \tag{6}$$

We do not normalize by histogram stretching, a common method to enhance contrast of the imagery, as it can result in detail reduction. We recognize, however, that some users may wish to increase contrast among midrange values. This can be done by users as an additional optional step. In this case σ^0_{min} and σ^0_{max} values that fall within the range of backscatter coefficient values are used to renormalize the image, "stretching" midrange values apart. The extreme high and low values less than σ^0_{min} or greater than σ^0_{max} are set to 0 and 1 respectively. Depending on the σ^0_{min} and σ^0_{max} values, this step can provide greater separation of midrange values and improve identification of low contrast features

https://doi.org/10.5194/egusphere-2026-4668
Preprint. Discussion started: 31 August 2026
© Author(s) 2026. CC BY 4.0 License.

(Q. Wang et al., 2016). It is also possible to over-enhance the image and reduce detail, particularly of bright features.

Finally, we reproject the image layers to an NSIDC northern hemisphere polar stereographic grid (EPSG:3413) (NSIDC, 2024; Qu et al., 2024; von Albedyll et al., 2024). Because sea ice is relatively flat and no digital elevation model is available, ellipsoid correction (ESA, 2024; Small & Schubert, 2008) and projection into geographic positions are used to reproject the image (part 1 step 3). Ellipsoid correction and projection are completed in the SNAP Sentinel Toolbox Application using the lookup file provided with the raw SAR download from ASF (ASF (Alaska Satellite Facility), 2024) of reference coordinates for each pixel in WGS84[278] (Part 1 step 3).

The final remote imagery data set contains a time series of Sentinel-1 images presented as speckle-reduced, radiometrically-calibrated backscatter coefficient values in HH and HV polarization and the cross-polarization ratio HH/HV, scaled in dB, normalized, and projected onto a polar stereographic reference system. These are intended to be input directly into the user's motion-extracting algorithm in the pairs identified by the acquisition times in the buoy data file (see buoy data Table 3 & Table 2).

We recognize that certain users may wish to preprocess the imagery in a different way. Therefore, we also include the original L1-GRD products. Preprocessing imagery from the raw L1-GRD through an alternate scheme is entirely "in bounds" for the challenge. Images can, for example, be resampled to set a particular pixel size (Demchev et al., 2017), contrast filtered (Figure 4, optional steps) (Song et al., 2021), or enhanced beyond histogram equalization with frequency domain image sharpening (Morrison et al., n.d.). Any additional filtering or enhancement should be performed before reprojection to prevent complications due to pixel shifting (ESA, 2024; Kusano et al., 2011).

We provide each SAR acquisition as a NetCDF file (general use -CF type) containing 6 layers: HH, HV, and HVHH ratio scaled in dB and from 0-1 (normalized). NetCDF is easily integrated into a variety of tools for machine-learning image processing, including pytorch (Jørgen Buus-Hinkler et al., 2022).

2.5. Image Sequences

A total of 28 images over the MOSAiC buoy array are preprocessed and combined into pairs from 2 January 2020 to 17 January 2020 (8 pairs) and 1 June 2020 to 20 June 2020 (11 pairs) and June 30, 2020 to 7 July 2020 6 pairs) with images separated by 1-4 days (Table 3). A total of 21 images over the SIDEx buoy array are preprocessed and combined into S1A pairs (6) and S1B pairs (13), spanning 14 March 2021 to 30 May 2021. Pair members are separated by 1-10 days (Table 2). The temporal separation of these pairs represent the range of typical intervals for SAR imagery repetition (1-10 days)

https://doi.org/10.5194/egusphere-2026-4668
Preprint. Discussion started: 31 August 2026
© Author(s) 2026. CC BY 4.0 License.

widely used for mapping sea ice motion at >10km scales (Kwok, 1996; Lindsay et al., 2003).

The images over the MOSAiC buoy array can be accessed at https://doi.pangaea.de/10.1594/PANGAEA.986430 (Kaidel, n.d.) and the images over the SIDEx buoy array can be access at https://doi.pangaea.de/10.1594/PANGAEA.994660 (Kaidel & Polashenski, n.d.).

Image pairs for the MOSAiC (Table 2) and SIDEx (Table 3) cases are presented with calculations of average buoy motion and number of buoys (n) that reported position in both images and remained within the images' boundaries. We also calculate relative displacement from one center buoy to all buoy-derived displacement vectors (Itkin, 2023; Nicolaus et al., 2022). The absolute value of the relative motion for the MOSAiC buoy array ranges from 0.0003 to 0.0045 m/s/m in January, from 0.0003 to 0.0086 m/s/m from June 1-20, 2020, and from 0.0008 to 0.0651 m/s/m in the first week of July. The absolute value of the relative motion for the SIDEx buoy array ranges from 0.000 to 0.0214 m/s/m, with the maximum relative motion occurring between April 18-20, 2021, despite a slightly slower than average drift speed of 0.0818 m/s (average= 0.086 m/s).

Image 1 time	Image 2 time	Buoy pairs (n)	Ice drift speed ($\lvert u_{x,y} \rvert$) [m/s]	Relative motion $\frac{du}{dx}$ [m/s/m]	Relative motion $\frac{dv}{dy}$ [m/s/m]
2020-01-02 at 03:27:29	2020-01-03 at 03:19:18	99	0.1638	-0.0045	0.0022
2020-01-03 at 03:19:18	2020-01-04 at 04:00:10	103	0.1105	0.0007	-0.0004
2020-01-04 at 04:00:10	2020-01-06 at 05:21:52	103	0.0731	0.0003	-0.0007
2020-01-06 at 05:21:52	2020-01-07 at 04:24:41	101	0.0358	0.0012	-0.0011
2020-01-07 at 04:24:41	2020-01-11 at 03:52:01	100	0.0608	0.0023	-0.0036
2020-01-11 at 03:52:01	2020-01-14 at 04:16:29	72	0.1466	0.0009	-0.0042
2020-01-14 at 04:16:29	2020-01-15 at 03:19:18	14	0.1117	-0.0086	0.0009
2020-01-15 at 03:19:18	2020-01-17 at 04:41:00	15	0.1141	-0.0169	0.0048
2020-06-01 at 07:27:02	2020-06-02 at 08:08:09	111	0.0625	-0.0012	0.0026
2020-06-02 at 08:08:09	2020-06-03 at 07:10:46	110	0.1079	-0.0034	0.0058
2020-06-03 at 07:10:46	2020-06-04 at 07:51:53	111	0.1308	-0.0083	0.0005
2020-06-04 at 07:51:53	2020-06-05 at 08:32:41	110	0.1546	-0.0086	0.0019
2020-06-05 at 08:32:41	2020-06-06 at 07:35:33	111	0.089	-0.0015	-0.0061
2020-06-06 at 07:35:33	2020-06-08 at 07:18:58	109	0.022	-0.0022	0.0021
2020-06-08 at 07:18:58	2020-06-10 at 07:02:35	109	0.1062	-0.0005	0.003
2020-06-10 at 07:02:35	2020-06-13 at 07:27:22	109	0.0548	-0.0021	0.0021
2020-06-13 at 07:27:22	2020-06-17 at 08:32:42	106	0.1494	-0.0023	0.006
2020-06-17 at 08:32:42	2020-06-19 at 08:16:22	106	0.0756	-0.0027	0.0024
2020-06-19 at 08:16:22	2020-06-20 at 07:19:02	106	0.0793	0.0003	-0.0035
2020-06-30 at 06:47:52	2020-07-02 at 07:20:02	18	0.0539	-0.0008	-0.0072

https://doi.org/10.5194/egusphere-2026-4668
Preprint. Discussion started: 31 August 2026
© Author(s) 2026. CC BY 4.0 License.

2020-07-02 at 07:20:02	2020-07-03 at 07:12:36	10	0.1908	0.0376	-0.0314
2020-07-03 at 07:12:36	2020-07-04 at 07:03:36	10	0.1478	0.0351	0.0113
2020-07-04 at 07:03:36	2020-07-05 at 07:44:37	39	0.0774	0.0147	0.0002
2020-07-05 at 07:44:37	2020-07-06 at 07:37:17	5	0.2211	0.0307	-0.0651
2020-07-06 at 07:37:17	2020-07-07 at 07:28:23	8	0.2379	0.0326	-0.078

Table 2. SAR image pairs for the MOSAiC cases

Image 1 time	Image 2 time	Buoy pairs (n)	Ice drift speed ($\lvert u_{x,y}\rvert$) [m/s]	Relative motion $\frac{du}{dx}$ [m/s/m]	Relative motion $\frac{dv}{dy}$ [m/s/m]
2021-03-13 at 16:58:35	2021-03-15 at 16:42:12	39	0.2396	-0.0139	0.026
2021-03-14 at 16:50:41	2021-03-16 at 16:34:12	43	0.251	0.0008	0.0001
2021-03-15 at 16:42:12	2021-03-25 at 16:58:35	42	0.0807	0.0008	0.0049
2021-03-16 at 16:34:12	2021-03-26 at 16:50:42	43	0.0583	0.0017	0.0014
2021-03-25 at 16:58:35	2021-03-27 at 16:42:13	41	0.0119	0.004	-0.0006
2021-03-26 at 16:50:42	2021-04-07 at 16:50:42	42	0.0497	0	0.0048
2021-03-27 at 16:42:13	2021-04-04 at 17:14:58	39	0.0802	0.0003	0.0079
2021-04-04 at 17:14:58	2021-04-06 at 16:58:36	40	0.01	-0.0007	-0.0008
2021-04-06 at 16:58:36	2021-04-11 at 17:06:47	28	0.0175	0.0013	0.0028
2021-04-07 at 16:50:42	2021-04-19 at 16:50:43	29	0.0125	-0.0079	0.0077
2021-04-11 at 17:06:47	2021-04-18 at 16:58:36	28	0.0278	-0.0107	0.0073
2021-04-18 at 16:58:36	2021-04-20 at 16:42:13	27	0.0818	-0.0036	0.0214
2021-04-19 at 16:50:43	2021-04-21 at 16:34:13	27	0.1095	0.0154	0.0098
2021-04-20 at 16:42:13	2021-04-23 at 17:06:48	27	0.0109	0.0017	0.0042
2021-04-21 at 16:34:13	2021-05-01 at 16:50:43	25	0.1256	-0.0111	0.0039
2021-04-23 at 17:06:48	2021-04-28 at 17:14:59	26	0.1523	-0.015	0.0057
2021-04-28 at 17:14:59	2021-04-30 at 16:58:37	24	0.1861	-0.0023	0.0128
2021-04-30 at 16:58:37	2021-05-03 at 17:23:11	24	0.0772	-0.0074	0.0145
2021-05-03 at 17:23:11	2021-05-05 at 17:06:48	23	0.0581	-0.0051	0.0144
2021-05-05 at 17:06:48	2021-05-30 at 17:47:47	20	0.0842	-0.0029	0.0092

Table 3. SAR image pairs for SIDEx case

3. Results

3.1. Reportable Metrics

We define a best practice for calculating the error of image-derived displacement fields using the provided buoy-derived displacement data and the presentation of that error. The purpose of defining a validation methodology is to standardize error

https://doi.org/10.5194/egusphere-2026-4668
Preprint. Discussion started: 31 August 2026
© Author(s) 2026. CC BY 4.0 License.

calculations to a degree that permits comparative evaluation of various approaches and advancement of the field.

While algorithm developers may choose any of a number of existing approaches (Bouillon & Rampal, 2015b; Fang et al., 2023b; S. E. L. Howell et al., 2022; Li et al., 2022; Muckenhuber et al., 2016; Thomas et al., 2011; X. Wang et al., 2022; Yang et al., 2024; X. Zhang et al., 2020) for extracting ice motion from the image pairs or develop new ones, the output should present the extracted sea ice motion as displacement vector maps, either feature-based or gridded. In feature-based maps, displacement vectors are located at non-gridded points, usually tied to a single pixel (S. Howell et al., 2022). Gridded motion maps, as implied, provide displacement in a regular spatial grid, often with each vector representing multiple pixels (Bouillon & Rampal, 2015a). Image-derived output should be an array of such absolute displacement vectors that follow the sign convention shown in Figure 5 and calculate magnitude (distance) and angle (direction) following Equation 7-Equation 9. Recognizing differences in approach, the vector array may have varying resolution and areas of coverage, though ideally it should target resolutions of at least 10 by 10 pixel area, or less than 0.5 km to be responsive.

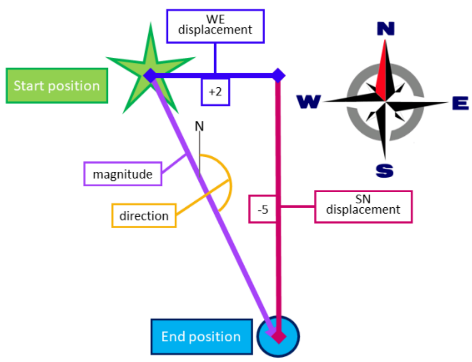

Figure 5. Demonstration of WE and SN displacement and magnitude and direction of a displacement vector.

$$\angle_a = \arctan\left(\frac{WE}{SN}\right) - 90^o \quad (7)$$

$$|v_a| = \sqrt{WE^2 + SN^2} \quad (8)$$

$$V = \frac{|v_a|}{t} \quad (9)$$

https://doi.org/10.5194/egusphere-2026-4668
Preprint. Discussion started: 31 August 2026
© Author(s) 2026. CC BY 4.0 License.

Where WE is the displacement in m from west to east in the EPSG:3413 projection (left to right) such that displacement from east to west (right to left) would be negative. SN is the displacement in map units from south to north (down to up) such that displacement from north to south (up to down) would be negative. The angle ($\angle_a$) calculated is in degrees clockwise from north.

We acknowledge that other types of motion mapping exist, such as damage and kinematic feature maps. (Hutter & Losch, 2020; Itkin, 2023) Methods for calculating the accuracy provided in these less common outputs depend on the unknown products and are left to the developers of these.

3.2. Calculating Accuracy

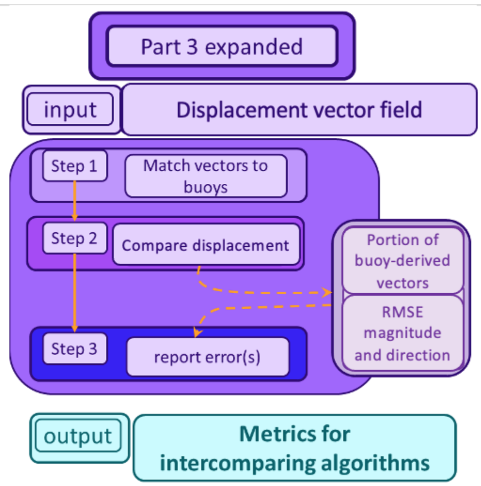

Figure 6. Part 3 of the challenge flow expanded to steps including matching algorithm vectors to buoy vectors, comparing velocities, and reporting error/accuracy.

Image-derived displacement vectors are next compared to the buoy-derived displacement vectors from drifting buoy arrays. Given the differences in resolution and location of image-derived displacement vectors, buoy-derived validation vectors likely do not coincide exactly in space with image derived estimates, and this spatial mismatch is different for every approach. Given the potential for differential displacement due to deformation, the greater the difference between positions, the more likely a mismatch is a real difference between motion at the two points rather than error in the image-derived vector. We prescribe criteria for selecting which image-derived vectors to compare to buoy-derived vectors, so that the differences from this are minimized. The selection criteria

https://doi.org/10.5194/egusphere-2026-4668
Preprint. Discussion started: 31 August 2026
© Author(s) 2026. CC BY 4.0 License.

are applicable to both feature based and gridded outputs and are intentionally simplistic to minimize inherently preferring one type of algorithm.

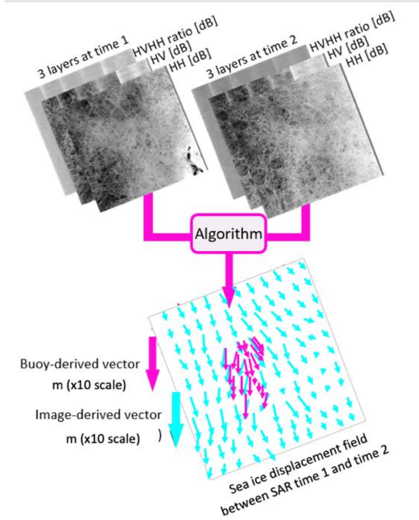

Figure 7. Example of a single image pair process taking in 2 images with 3 layers and outputting an image-derived motion map

To select image-derived displacement vectors for comparison to buoy-derived validation vectors we use a simple proximity criterion. We set a window around each buoy-derived vector, and compare the closest image-derived vector within this spatial window (S. Howell et al., 2022). We set a window of 3x3 km (or 75x75 pixels) centered on a buoy-derived vector, similar to Howell et al. (S. Howell et al., 2022) If there are multiple image-derived vectors within this spatial window, only the nearest image-derived vector in this window is directly compared to the buoy-derived vector. (Figure 8a). This is done, rather than interpolation, because in cases where interpolation would include vectors of differing magnitude, this is ultimately due to a discrete discontinuity in the ice within the vectors (e.g., two separate floes). Averaging displacement of adjacent floes has less merit than seeking to maximize likelihood of comparing a point on the same floe (closest point). In the case where there is no acceptable image-derived vector to compare to a provided buoy-derived vector, this should be recorded and reported on in the total portion of buoy-derived displacement vectors compared (Equation 11).

https://doi.org/10.5194/egusphere-2026-4668
Preprint. Discussion started: 31 August 2026
© Author(s) 2026. CC BY 4.0 License.

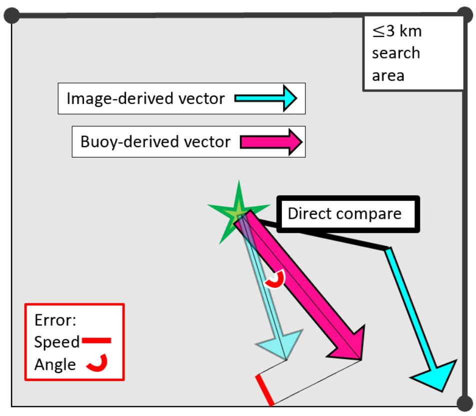

Figure 8. Approach to validating image-derived motion from feature-based algorithm output

$$f_b = \frac{N_c}{N_b} \tag{10}$$

$$F_b = \frac{\sum f_b}{N_I} \tag{11}$$

Where f_b is the fraction of buoy-derived vectors compared for a single image pair, N_c is the number of buoy-derived vectors compared to corresponding image-derived vectors, and N_b is the total number of buoy-derived vectors within the image extent. F_b is the average portion of buoy-derived vectors compared across image pairs in one of the four case study periods (SIDEx, MOSAiC January, June, and July), and is the sum of each image pair fraction (f_b) divided by the total number of image pairs in the case (N_I). The fraction of buoy-derived vectors compared indicates how much of an image was validated with buoy-derived displacement vectors. A high proportion of buoy-derived vectors compared with a low RMSE value indicates high confidence, compared to a low proportion of buoy-derived vectors compared with a similar RMSE value. For point-based motion-extracting algorithms, F_b will depend on the density and uniformity in spacing of successfully mapped points. For gridded output F_b will depend on the density of the output motion field.

Once image-derived vectors are selected and matched to buoy-derived vectors, the displacement can be compared. Vector pairs are used to calculate the average root mean squared error (RMSE) (Equation 12- Equation 13):

https://doi.org/10.5194/egusphere-2026-4668
Preprint. Discussion started: 31 August 2026
© Author(s) 2026. CC BY 4.0 License.

$$RMSE = \sqrt{\sum_{i=1}^{n} \frac{(|d_b| - |d_a|)^2}{n}} \tag{12}$$

$$RMSE = \sqrt{\sum_{i=1}^{n} \frac{(\angle_b - \angle_a)^2}{n}} \tag{13}$$

Where d_b/d_a are the displacement in m/s and $\angle_b/\angle_a$ clockwise direction in degrees from north of the buoy-derived vector and the image-derived vector. The value n is an integer representing the total number vector pairs used to calculate the RMSE.

4. "Submission"

Comparison between algorithms using this standardized challenge dataset is intended to be an open and distributed process carried out in the literature – that is to say there is no location to centrally collect submissions. We encourage others to use the data provided here to test their approach and to include the metrics calculated above when publishing an algorithm, so that others may easily compare algorithm performance. For reporting, we encourage users, at a minimum, to include a table and plotset. The table should list the average RMSE for magnitude (displacement) and angle (direction) and the portion of buoy-derived vectors compared to image-derived vectors (F_b) for each of the four test cases (SIDEx and MOSAiC January, June, and July), as in Figure 9. The plotset should depict a scatterplot of buoy derived vs. image derived vector magnitude and direction showing RMSE and portion of buoy-derived validation vectors used (Figure 11).

https://doi.org/10.5194/egusphere-2026-4668
Preprint. Discussion started: 31 August 2026
© Author(s) 2026. CC BY 4.0 License.

	Metrics for Comparing algorithm performance	
	Metric	Value
Case 1 (SIDEx)	RMSE magnitude	
	RMSE angle	
	F_b	
Case 2 (MOSAiC Jan)	RMSE magnitude	
	RMSE angle	
	F_b	
Case 3 (MOSAiC June)	RMSE magnitude	
	RMSE angle	
	F_b	
Case 4 (MOSAiC July)	RMSE magnitude	
	RMSE angle	
	F_b	

Figure 9. Blank table showing motion-extracting algorithm evaluation metrics to be reported for each case (SIDEx, MOSAiC January, June, and July), for either feature-based output or gridded output.

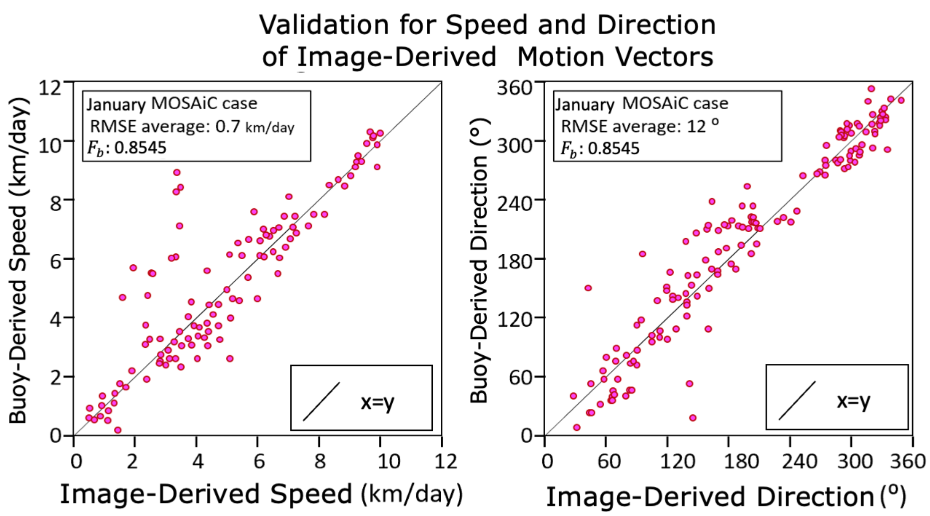

Figure 10. Example of key figure comparing image-derived motion to buoy-derived motion for validation and error metric (RMSE) for speed (magnitude) and direction (angle)

5. Conclusion

We provide an open-access dataset package for testing algorithms that extract sea ice motion estimates from sequential SAR imagery, removing barriers to developing and testing new algorithms as well as enhancing intercomparisons between methods. The open challenge is intended to enable those without prior knowledge of sea ice dynamics to contribute to the goal of higher resolution automated sea ice motion. The datasets include

https://doi.org/10.5194/egusphere-2026-4668
Preprint. Discussion started: 31 August 2026
© Author(s) 2026. CC BY 4.0 License.

preprocessed SAR imagery for inputs to reduce time spent on data wrangling and preparation for future development. Preprocessed imagery is provided in a commonly used format (NetCDF) along with an image file compatible with the SNAP toolbox (BEAM-DIMAP), and L1-GRD products to provide points of entry for users with different approaches. Buoy-derived motion data are provided for accuracy calculations which require no further manipulation of in situ data. A best practice validation method is outlined to facilitate direct and easy intercomparison between image-derived motion maps by creating a standard table and figure. The case studies are chosen over the densest sea ice buoy validation arrays recently available and represent varied seasonal (winter, spring, summer) and dynamic conditions (closed ice pack, coastal shear, opening ice pack). We look forward to contributions from the interdisciplinary sea ice community and other fields of expertise.

6. Data availability

The two datasets of original L1 SAR images and processed images are published on Pangea (https://doi.pangaea.de/10.1594/PANGAEA.994660, https://doi.pangaea.de/10.1594/PANGAEA.986430), referencing the MOSAiC and SIDEx case studies, respectively. The buoy data are included in the supplemental tables of this manuscript as a .zip file.

7. Author contributions

CP conceptualized the community challenge idea and identified data sources for satellite images and buoy data. LK and CP developed the methodology. LK processed all data, including satellite images, created all images, and wrote the first draft of the paper with contributions from CP.

https://doi.org/10.5194/egusphere-2026-4668
Preprint. Discussion started: 31 August 2026
© Author(s) 2026. CC BY 4.0 License.

References

ASF (Alaska Satellite Facility). (2024). *Alaska Satellite Facility Distributed Active Archive Center* [Archive]. https://www.earthdata.nasa.gov/centers/asf-daac

ASFS. (n.d.). *Atmospheric Surface Flux Station: NOAA Physical Sciences Laboratory*. Retrieved February 9, 2026, from https://www.psl.noaa.gov/technology/asfs/

Attema, E., Snoeij, P., Davidson, M., Floury, N., Levrini, G., Romman, B., & Rosich, B. (2008). The European GMES Sentinel-1 Radar Mission. *ResearchGate*. https://doi.org/10.1109/IGARSS.2008.4778801

Bay, H., Tuytelaars, T., & Van Gool, L. (2006). SURF: Speeded Up Robust Features. In A. Leonardis, H. Bischof, & A. Pinz (Eds.), *Computer Vision – ECCV 2006* (pp. 404–417). Springer. https://doi.org/10.1007/11744023_32

Bi, H., Liang, Y., Wang, Y., Liang, X., Zhang, Z., Du, T., Yu, Q., Huang, J., Kong, M., & Huang, H. (2020). Arctic multiyear sea ice variability observed from satellites: A review. *Journal of Oceanology and Limnology*, *38* (4), 962–984. https://doi.org/10.1007/s00343-020-0093-7

Bliss, A., Hutchings, J., Anderson, P., Anhaus, P., Belter, H. J., Berge, J., Bessonov, V., Cheng, B., Cole, S., Costa, D., Cottier, F., Cox, C. J., Torre, P. R. D. L., Divine, D. V., Emzivat, G., Fang, Y.-C., Fons, S., Gallagher, M., Geoffrey, M., … Zuo, G. (2022). *Sea ice drift tracks from the Distributed Network of autonomous buoys deployed during the Multidisciplinary drifting Observatory for the Study of Arctic Climate (MOSAiC) expedition 2019—2021*. https://doi.org/10.18739/A2KP7TS83

Bouchat, A., Hutter, N., Chanut, J., Dupont, F., Dukhovskoy, D., Garric, G., Lee, Y. J., Lemieux, J.-F., Lique, C., Losch, M., Maslowski, W., Myers, P. G., Ólason, E., Rampal, P., Rasmussen, T., Talandier, C., Tremblay, B., & Wang, Q. (2022). Sea

https://doi.org/10.5194/egusphere-2026-4668
Preprint. Discussion started: 31 August 2026
© Author(s) 2026. CC BY 4.0 License.

Ice Rheology Experiment (SIREx): 1. Scaling and Statistical Properties of Sea-Ice Deformation Fields. *Journal of Geophysical Research: Oceans*, *127* (4), e2021JC017667. https://doi.org/10.1029/2021JC017667

Bouillon, S., & Rampal, P. (2015a). On producing sea ice deformation data sets from SAR-derived sea ice motion. *The Cryosphere*, *9* (2), 663–673. https://doi.org/10.5194/tc-9-663-2015

Bouillon, S., & Rampal, P. (2015b). On producing sea ice deformation data sets from SAR-derived sea ice motion. *The Cryosphere*, *9* (2), 663–673. https://doi.org/10.5194/tc-9-663-2015

Brandt, F., Disser, K., Haller-Dintelmann, R., & Hieber, M. (2022). Rigorous Analysis and Dynamics of Hibler's Sea Ice Model. *Journal of Nonlinear Science*, *32* (4), 50. https://doi.org/10.1007/s00332-022-09805-w

Castriotta, A. G. (2022). *Copernicus Sentinel Data Access Annual Report Y2021* (COPE-SERCO-RP-22-1312; p. 129). SERCO public.

Copernicus, & ESA, E. S. A. (2022). *Contributing Missions Online* [Data overview]. Copernicus Contributing Missions Online. https://spacedata.copernicus.eu

Curlander, J., Holt, B., & Hussey, K. (1985). Determination of sea ice motion using digital SAR imagery. *IEEE Journal of Oceanic Engineering*, *10* (4), 358–367. IEEE Journal of Oceanic Engineering. https://doi.org/10.1109/JOE.1985.1145134

Demchev, D., Volkov, V., Kazakov, E., Alcantarilla, P. F., Sandven, S., & Khmeleva, V. (2017). Sea Ice Drift Tracking From Sequential SAR Images Using Accelerated-KAZE Features. *IEEE Transactions on Geoscience and Remote Sensing*, *55* (9),

https://doi.org/10.5194/egusphere-2026-4668
Preprint. Discussion started: 31 August 2026
© Author(s) 2026. CC BY 4.0 License.

5174–5184. IEEE Transactions on Geoscience and Remote Sensing. https://doi.org/10.1109/TGRS.2017.2703084

EarthData, & VITO, F. I. for T. R. (2021). *Sentinel-1 Level-1 Ground Range Detected (GRD) products.* (Nos. C2207478611-FEDEO; Version 1) [Dataset]. https://cmr.earthdata.nasa.gov/search/concepts/C2207478611-FEDEO.html

ESA, E. S. A. (2024). *Science Toolbox Exploitation Platform—SNAP* (Version 11.0.0) [Documentation]. https://step.esa.int/main/doc/online-help/

ESA, E. S. A. (2025, February 6). *From launch to images: The roadmap to Sentinel-1C operations*. Sentinel Online. https://sentinels.copernicus.eu/-/from-launch-to-images-the-roadmap-to-sentinel-1c-operations

ESA, E. S. A., & Copernicus. (2024). *S1 Mission*. European Space Agency. https://sentiwiki.copernicus.eu/web/s1-mission#S1-Mission-Acquisition-Modes

Fang, Y., Wang, X., Li, G., Chen, Z., Hui, F., & Cheng, X. (2023a). Arctic sea ice drift fields extraction based on feature tracking to MODIS imagery. *International Journal of Applied Earth Observation and Geoinformation*, *120*, 103353. https://doi.org/10.1016/j.jag.2023.103353

Fang, Y., Wang, X., Li, G., Chen, Z., Hui, F., & Cheng, X. (2023b). Arctic sea ice drift fields extraction based on feature tracking to MODIS imagery. *International Journal of Applied Earth Observation and Geoinformation*, *120*, 103353. https://doi.org/10.1016/j.jag.2023.103353

Feltham, D. L. (2008). Sea Ice Rheology. *Annual Review of Fluid Mechanics*, *40* (Volume 40, 2008), 91–112. https://doi.org/10.1146/annurev.fluid.40.111406.102151

© Author(s) 2026. CC BY 4.0 License.

Fily, M., & Rothrock, D. A. (1986). Extracting Sea Ice Data from Satellite SAR Imagery. *IEEE Transactions on Geoscience and Remote Sensing*, *GE-24* (6), 849–854. IEEE Transactions on Geoscience and Remote Sensing. https://doi.org/10.1109/TGRS.1986.289699

Gao, J., Jiang, H., Sun, Z., Wang, R., & Han, Y. (2023). A Parallel InSAR Phase Unwrapping Method Based on Separated Continuous Regions. *Remote Sensing*, *15* (5), Article 5. https://doi.org/10.3390/rs15051370

Geudtner, D., Torres, R., Snoeij, P., Davidson, M., & Rommen, B. (2014). Sentinel-1 System capabilities and applications. *2014 IEEE Geoscience and Remote Sensing Symposium*, 1457–1460. https://doi.org/10.1109/IGARSS.2014.6946711

Girard, L., Weiss, J., Molines, J. M., Barnier, B., & Bouillon, S. (2009). Evaluation of high-resolution sea ice models on the basis of statistical and scaling properties of Arctic sea ice drift and deformation. *Journal of Geophysical Research: Oceans*, *114* (C8). https://doi.org/10.1029/2008JC005182

Goyal, M. (2011). *Morphological Image Processing*. *2* (4), 59.

Graham, R. M., Itkin, P., Meyer, A., Sundfjord, A., Spreen, G., Smedsrud, L. H., Liston, G. E., Cheng, B., Cohen, L., Divine, D., Fer, I., Fransson, A., Gerland, S., Haapala, J., Hudson, S. R., Johansson, A. M., King, J., Merkouriadi, I., Peterson, A. K., … Granskog, M. A. (2019). Winter storms accelerate the demise of sea ice in the Atlantic sector of the Arctic Ocean. *Scientific Reports*, *9* (1), Article 1. https://doi.org/10.1038/s41598-019-45574-5

https://doi.org/10.5194/egusphere-2026-4668
Preprint. Discussion started: 31 August 2026
© Author(s) 2026. CC BY 4.0 License.

Guaragnella, C., & D'Orazio, T. (2019). A Data-Driven Approach to SAR Data-Focusing. *Sensors (Basel, Switzerland)*, *19* (7), 1649. https://doi.org/10.3390/s19071649

Hajduch, G., & Bourbigot, M. (2021). *Sentinel-1 Product Specification* (Specifications Nos. S1-RS-MDA-52–7441; Sentinel-1). ESA.

Howell, S., Brady, M., & Komarov, A. S. (2022, December 13). *Generating pan-Arctic sea ice motion from synthetic aperture radar using the Environment and Climate Change Canada automated sea ice tracking system*. Fall Meeting 2022. https://agu.confex.com/agu/fm22/meetingapp.cgi/Paper/1048851

Howell, S. E. L., Brady, M., & Komarov, A. S. (2022). Generating large-scale sea ice motion from Sentinel-1 and the RADARSAT Constellation Mission using the Environment and Climate Change Canada automated sea ice tracking system. *The Cryosphere*, *16* (3), 1125–1139. https://doi.org/10.5194/tc-16-1125-2022

Howell, S. E. L., Komarov, A. S., Dabboor, M., Montpetit, B., Brady, M., Scharien, R. K., Mahmud, M. S., Nandan, V., Geldsetzer, T., & Yackel, J. J. (2018). Comparing L- and C-band synthetic aperture radar estimates of sea ice motion over different ice regimes. *Remote Sensing of Environment*, *204*, 380–391. https://doi.org/10.1016/j.rse.2017.10.017

Hutchings, J. K., Roberts, A., Geiger, C. A., & Richter-Menge, J. (2011). Spatial and temporal characterization of sea-ice deformation. *Annals of Glaciology*, *52* (57), 360–368. https://doi.org/10.3189/172756411795931769

https://doi.org/10.5194/egusphere-2026-4668
Preprint. Discussion started: 31 August 2026
© Author(s) 2026. CC BY 4.0 License.

Hutter, N., & Losch, M. (2020). Feature-based comparison of sea ice deformation in lead-permitting sea ice simulations. *The Cryosphere*, *14* (1), 93–113. https://doi.org/10.5194/tc-14-93-2020

iSVP. (n.d.). *MetOcean Telematics*. Retrieved February 9, 2026, from https://metocean.com/products/isvp/

Itkin, P. (2023). Novel methods to study sea ice deformation, linear kinematic features and coherent dynamic elements from imaging remote sensing data. *EGUsphere*, 1–26. https://doi.org/10.5194/egusphere-2023-2626

Itkin, P., Spreen, G., Cheng, B., Doble, M., Girard-Ardhuin, F., Haapala, J., Hughes, N., Kaleschke, L., Nicolaus, M., & Wilkinson, J. (2017). Thin ice and storms: Sea ice deformation from buoy arrays deployed during N-ICE2015. *Journal of Geophysical Research: Oceans*, *122* (6), 4661–4674. https://doi.org/10.1002/2016JC012403

Jørgen Buus-Hinkler, Tore Wulf, Andreas Rønne Stokholm, Anton Korosov, Roberto Saldo, Leif Toudal Pedersen, David Arthurs, Rune Solberg, Nicolas Longépé, & Matilde Brandt Kreiner. (2022). *Raw AI4Arctic Sea Ice Challenge Test Dataset* [Dataset]. Technical University of Denmark. https://doi.org/10.11583/DTU.21762848.v1

Kaidel, L. (n.d.). *Synthetic Aperture Radar Images from Sentinel-1 over the Arctic Ocean and Fram Strait from January 2020, June 2020, and July 2020* [Dataset]. PANGAEA. Retrieved July 24, 2026, from https://doi.pangaea.de/10.1594/PANGAEA.994660

https://doi.org/10.5194/egusphere-2026-4668
Preprint. Discussion started: 31 August 2026
© Author(s) 2026. CC BY 4.0 License.

Kaidel, L., & Polashenski, C. (n.d.). *Synthetic Aperture Radar Images from Sentinel-1 over the Arctic Ocean from 2020-2021* [Dataset]. PANGAEA. Retrieved July 24, 2026, from https://doi.pangaea.de/10.1594/PANGAEA.986430

Karvonen, J. (2014). Baltic Sea Ice Concentration Estimation Based on C-Band Dual-Polarized SAR Data. *IEEE Transactions on Geoscience and Remote Sensing*, *52* (9), 5558–5566. IEEE Transactions on Geoscience and Remote Sensing. https://doi.org/10.1109/TGRS.2013.2290331

Komarov, A. S., & Barber, D. G. (2014). Sea Ice Motion Tracking From Sequential Dual-Polarization RADARSAT-2 Images. *IEEE Transactions on Geoscience and Remote Sensing*, *52* (1), 121–136. IEEE Transactions on Geoscience and Remote Sensing. https://doi.org/10.1109/TGRS.2012.2236845

Korosov, A. A., & Rampal, P. (2017). A Combination of Feature Tracking and Pattern Matching with Optimal Parametrization for Sea Ice Drift Retrieval from SAR Data. *Remote Sensing*, *9* (3), Article 3. https://doi.org/10.3390/rs9030258

Korosov, A., Rampal, P., Ying, Y., Ólason, E., & Williams, T. (2023). Towards improving short-term sea ice predictability using deformation observations. *The Cryosphere*, *17* (10), 4223–4240. https://doi.org/10.5194/tc-17-4223-2023

Krumpen, T., von Albedyll, L., Goessling, H. F., Hendricks, S., Juhls, B., Spreen, G., Willmes, S., Belter, H. J., Dethloff, K., Haas, C., Kaleschke, L., Katlein, C., Tian-Kunze, X., Ricker, R., Rostosky, P., Rückert, J., Singha, S., & Sokolova, J. (2021). MOSAiC drift expedition from October 2019 to July 2020: Sea ice conditions from space and comparison with previous years. *The Cryosphere*, *15* (8), 3897–3920. https://doi.org/10.5194/tc-15-3897-2021

https://doi.org/10.5194/egusphere-2026-4668
Preprint. Discussion started: 31 August 2026
© Author(s) 2026. CC BY 4.0 License.

Kusano, S., Sato, M., & Yokota, Y. (2011). Data interpolation and resampling for a synthetic aperture radar data. *2011 IEEE International Geoscience and Remote Sensing Symposium*, 652–655. https://doi.org/10.1109/IGARSS.2011.6049213

Kwok, R. (1996). *The RADARSAT Geophysical Processor System* (Version 2) [Dataset]. JPL open repo. https://dataverse.jpl.nasa.gov/file.xhtml?fileId=30557&version=2.0&toolType=PREVIEW. https://hdl.handle.net/2014/27703

Kwok, R. (2002). Sea ice concentration estimates from satellite passive microwave radiometry and openings from SAR ice motion. *Geophysical Research Letters*, *29* (9), 25-1-25–4. https://doi.org/10.1029/2002GL014787

Kwok, R., & Cunningham, G. F. (2002). Seasonal ice area and volume production of the Arctic Ocean: November 1996 through April 1997. *Journal of Geophysical Research: Oceans*, *107* (C10), SHE 12-1-SHE 12-17. https://doi.org/10.1029/2000JC000469

Kwok, R., Cunningham, G. F., & Pang, S. S. (2004). Fram Strait sea ice outflow. *Journal of Geophysical Research: Oceans*, *109* (C1). https://doi.org/10.1029/2003JC001785

Kwok, R., Spreen, G., & Pang, S. (2013). Arctic sea ice circulation and drift speed: Decadal trends and ocean currents. *Journal of Geophysical Research: Oceans*, *118* (5), 2408–2425. https://doi.org/10.1002/jgrc.20191

Laur, H., Bally, P., Meadows, P., Sanchez, J., Schaettler, B., Lopinto, E., & Esteban, D. (2002). Derivation of the backscattering coefficient σ0 in ESA ERS SAR PRI products. *Second International Workshop on ERS Applications*.

https://doi.org/10.5194/egusphere-2026-4668
Preprint. Discussion started: 31 August 2026
© Author(s) 2026. CC BY 4.0 License.

Lee, J.-S., Grunes, M. R., & de Grandi, G. (1999). Polarimetric SAR speckle filtering and its implication for classification. *IEEE Transactions on Geoscience and Remote Sensing*, *37* (5), 2363–2373. IEEE Transactions on Geoscience and Remote Sensing. https://doi.org/10.1109/36.789635

Lee, J.-S., Wen, J.-H., Ainsworth, T. L., Chen, K.-S., & Chen, A. J. (2009). Improved Sigma Filter for Speckle Filtering of SAR Imagery. *IEEE Transactions on Geoscience and Remote Sensing*, *47* (1), 202–213. IEEE Transactions on Geoscience and Remote Sensing. https://doi.org/10.1109/TGRS.2008.2002881

Li, M. C., Zhou, C. X., Li, B., Chen, X. L., Liu, J. Q., & Zeng, T. (2022). Application of the combined feature tracking and maximum cross-correlation algorithm to the extraction of sea ice motion data from GF-3 imagery. *IEEE J. Sel. Top. Appl. Earth Observ. Remote Sens.*, *15*, 3390–3402. https://doi.org/10.1109/JSTARS.2022.3166897

Liew, S. C. (2001). *Principles of Remote Sensing—Centre for Remote Imaging, Sensing and Processing, CRISP*. https://crisp.nus.edu.sg/~research/tutorial/sar_int.htm

Lindsay, R. W., Zhang, J., & Rothrock, D. A. (2003). Sea-ice deformation rates from satellite measurements and in a model. *Atmosphere-Ocean*, *41* (1), 35–47. https://doi.org/10.3137/ao.410103

Liu, Y., Key, J. R., Wang, X., & Tschudi, M. (2020). Multidecadal Arctic sea ice thickness and volume derived from ice age. *The Cryosphere*, *14* (4), 1325–1345. https://doi.org/10.5194/tc-14-1325-2020

Lowe, G. (2004). *Sift-the scale invariant feature transform*. *2* (91–110), 2.

https://doi.org/10.5194/egusphere-2026-4668
Preprint. Discussion started: 31 August 2026
© Author(s) 2026. CC BY 4.0 License.

Maeda, K., Kimura, N., & Yamaguchi, H. (2020). Temporal and spatial change in the relationship between sea-ice motion and wind in the Arctic. *Polar Research*. https://doi.org/10.33265/polar.v39.3370

Marsan, D., Stern, H., Lindsay, R., & Weiss, J. (2004). Scale Dependence and Localization of the Deformation of Arctic Sea Ice. *Physical Review Letters*, *93* (17), 178501. https://doi.org/10.1103/PhysRevLett.93.178501

Morrison, R., Do, M., & Munson, D. (n.d.). *SAR Image Autofocus By Sharpness Optimization: A Theoretical Study*.

Muckenhuber, S., Korosov, A. A., & Sandven, S. (2016). Open-source feature-tracking algorithm for sea ice drift retrieval from Sentinel-1 SAR imagery. *The Cryosphere*, *10* (2), 913–925. https://doi.org/10.5194/tc-10-913-2016

Naval Postgraduate School. (n.d.). *Autonomous Ocean Flux Buoy Program*. Retrieved February 9, 2026, from https://www.oc.nps.edu/~stanton/fluxbuoy/

Nicolaus, M., Perovich, D. K., Spreen, G., Granskog, M. A., von Albedyll, L., Angelopoulos, M., Anhaus, P., Arndt, S., Belter, H. J., Bessonov, V., Birnbaum, G., Brauchle, J., Calmer, R., Cardellach, E., Cheng, B., Clemens-Sewall, D., Dadic, R., Damm, E., de Boer, G., … Wendisch, M. (2022). Overview of the MOSAiC expedition: Snow and sea ice. *Elementa: Science of the Anthropocene*, *10* (1), 000046. https://doi.org/10.1525/elementa.2021.000046

NSIDC. (2024). *A Guide to NSIDC's Polar Stereographic Projection*. National Snow and Ice Data Center. https://nsidc.org/data/user-resources/help-center/guide-nsidcs-polar-stereographic-projection

https://doi.org/10.5194/egusphere-2026-4668
Preprint. Discussion started: 31 August 2026
© Author(s) 2026. CC BY 4.0 License.

Oikkonen, A., Haapala, J., Lensu, M., & Karvonen, J. (2016). Sea ice drift and deformation in the coastal boundary zone. *Geophysical Research Letters*, *43* (19), 10,303-10,310. https://doi.org/10.1002/2016GL069632

Pacific Gyre. (2024). *Lagrangian Drifters* [Dataset]. https://www.pacificgyre.com/products.aspx

Perovich, D., & Polashenski, C. (2024). *Sea ice mass balance (SIMB) data from The Sea Ice Dynamics Experiment (SIDEX); Beaufort Gyre, 2021* [Dataset]. Arctic Data Center. https://doi.org/10.18739/A2B27PS9J

Potin, P., Gascon, F., Stromme, A., Zehner, C., Wilson, H., Figa, J., Obligis, E., & Lindstrot, R. (2021). *Sentinel High Level Operations Plan (HLOP)* (PL COPE-S1OP-EOPG-PL-15-0020). Copernicus Space Component Mission Management Team. chrome-extension://efaidnbmnnnibpcajpcglclefindmkaj/https://sentiwiki.copernicus.eu/__attachments/1673407/COPE-S1OP-EOPG-PL-15-0020%20-%20Sentinel%20HLOP%202021%20-%203.1.pdf?inst-v=b5b6d4e4-2c90-49eb-84a7-a94cd264a04f

Qu, M., Lei, R., Liu, Y., & Li, N. (2024). Arctic Sea ice leads detected using sentinel-1B SAR image and their responses to atmosphere circulation and sea ice dynamics. *Remote Sensing of Environment*, *308*, 114193. https://doi.org/10.1016/j.rse.2024.114193

Rampal, P., Weiss, J., & Marsan, D. (2009). Positive trend in the mean speed and deformation rate of Arctic sea ice, 1979–2007. *Journal of Geophysical Research: Oceans*, *114* (C5). https://doi.org/10.1029/2008JC005066

Rampal, P., Weiss, J., Marsan, D., & Bourgoin, M. (2009). Arctic sea ice velocity field: General circulation and turbulent-like fluctuations. *Journal of Geophysical Research: Oceans*, *114* (C10). https://doi.org/10.1029/2008JC005227

Reddy, B. S., & Chatterji, B. N. (1996). An FFT-based technique for translation, rotation, and scale-invariant image registration. *IEEE Transactions on Image Processing*, *5* (8), 1266–1271. IEEE Transactions on Image Processing. https://doi.org/10.1109/83.506761

Rheinlænder, J. W., Davy, R., Ólason, E., Rampal, P., Spensberger, C., Williams, T. D., Korosov, A., & Spengler, T. (2022a). Driving Mechanisms of an Extreme Winter Sea Ice Breakup Event in the Beaufort Sea. *Geophysical Research Letters*, *49* (12), e2022GL099024. https://doi.org/10.1029/2022GL099024

Rheinlænder, J. W., Davy, R., Ólason, E., Rampal, P., Spensberger, C., Williams, T. D., Korosov, A., & Spengler, T. (2022b). Driving Mechanisms of an Extreme Winter Sea Ice Breakup Event in the Beaufort Sea. *Geophysical Research Letters*, *49* (12), Article 12. https://doi.org/10.1029/2022GL099024

Riccardo Piantanida. (2022). *Sentinel-1 Level 1 Detailed Algorithm Definition* (SEN-TN-52-7445; Sentinel-1).

Ringeisen, D., Hutter, N., & von Albedyll, L. (2023). Deformation lines in Arctic sea ice: Intersection angle distribution and mechanical properties. *The Cryosphere*, *17* (9), 4047–4061. https://doi.org/10.5194/tc-17-4047-2023

Royal Institute of Navigation. (1972). *The Journal of navigation*. Royal Institute of Navigation.

https://doi.org/10.5194/egusphere-2026-4668
Preprint. Discussion started: 31 August 2026
© Author(s) 2026. CC BY 4.0 License.

S. Quegan, T. L. Toan, J. J. Yu, F. Ribbes, & N. Floury. (2000). Multitemporal ERS SAR Analysis Applied to Forest Mapping. *IEEE Transactions on Geoscience and Remote Sensing*, *38* (2).

SAMS Enterprise. (n.d.). *SIMBA — SAMS Enterprise—Marine Consultancy*. Retrieved February 9, 2026, from https://www.sams-enterprise.com/products/simba/

SATICE, Elosegui, P., & Wilkinson, J. (2014). *SATICE a high-precision GPS autonomous platform* [Product]. http://satice.icm.csic.es/

Serreze, M. C., & Stroeve, J. (2015). Arctic sea ice trends, variability and implications for seasonal ice forecasting. *Philosophical Transactions of the Royal Society A: Mathematical, Physical and Engineering Sciences*, *373* (2045), 20140159. https://doi.org/10.1098/rsta.2014.0159

Shokr, M., & Sinha, N. K. (2023). *Sea Ice: Physics and Remote Sensing*. John Wiley & Sons.

Small, D. (2011). Flattening Gamma: Radiometric Terrain Correction for SAR Imagery. *IEEE Transactions on Geoscience and Remote Sensing*, *49* (8), 3081–3093. IEEE Transactions on Geoscience and Remote Sensing. https://doi.org/10.1109/TGRS.2011.2120616

Small, D., & Schubert, A. (2008). *Guide to ASAR geocoding* (Technical Note RSL-ASAR-GC-AD 1; p. 36). ESA-ESRIN.

Song, W., Li, M., Gao, W., Huang, D., Ma, Z., Liotta, A., & Perra, C. (2021). Automatic Sea-Ice Classification of SAR Images Based on Spatial and Temporal Features Learning. *IEEE Transactions on Geoscience and Remote Sensing*, *59* (12), 9887–

https://doi.org/10.5194/egusphere-2026-4668
Preprint. Discussion started: 31 August 2026
© Author(s) 2026. CC BY 4.0 License.

9901. IEEE Transactions on Geoscience and Remote Sensing. https://doi.org/10.1109/TGRS.2020.3049031

Spreen, G., Kwok, R., & Menemenlis, D. (2011). Trends in Arctic sea ice drift and role of wind forcing: 1992–2009. *Geophysical Research Letters*, *38* (19). https://doi.org/10.1029/2011GL048970

Spreen, G., Kwok, R., Menemenlis, D., & Nguyen, A. T. (2017). Sea-ice deformation in a coupled ocean–sea-ice model and in satellite remote sensing data. *The Cryosphere*, *11* (4), 1553–1573. https://doi.org/10.5194/tc-11-1553-2017

Stern, H. L., & Lindsay, R. W. (2009a). Spatial scaling of Arctic sea ice deformation. *Journal of Geophysical Research: Oceans*, *114* (C10). https://doi.org/10.1029/2009JC005380

Stern, H. L., & Lindsay, R. W. (2009b). Spatial scaling of Arctic sea ice deformation. *Journal of Geophysical Research: Oceans*, *114* (C10). https://doi.org/10.1029/2009JC005380

SUN, Y. (1996). Automatic ice motion retrieval from ERS-1 SAR images using the optical flow method. *International Journal of Remote Sensing*, *17* (11), 2059–2087. https://doi.org/10.1080/01431169608948759

Tan, W., Li, J., Xu, L., & Chapman, M. A. (2018). Semiautomated Segmentation of Sentinel-1 SAR Imagery for Mapping Sea Ice in Labrador Coast. *IEEE Journal of Selected Topics in Applied Earth Observations and Remote Sensing*, *11* (5), 1419–1432. IEEE Journal of Selected Topics in Applied Earth Observations and Remote Sensing. https://doi.org/10.1109/JSTARS.2018.2806640

https://doi.org/10.5194/egusphere-2026-4668
Preprint. Discussion started: 31 August 2026
© Author(s) 2026. CC BY 4.0 License.

Thomas, M., Kambhamettu, C., & Geiger, C. A. (2011). Motion Tracking of Discontinuous Sea Ice. *IEEE Transactions on Geoscience and Remote Sensing*, *49* (12), 5064–5079. IEEE Transactions on Geoscience and Remote Sensing. https://doi.org/10.1109/TGRS.2011.2158005

Toyota, T., Ishiyama, J., & Kimura, N. (2021). Measuring Deformed Sea Ice in Seasonal Ice Zones Using L-Band SAR Images. *IEEE Transactions on Geoscience and Remote Sensing*, *59* (11), 9361–9381. IEEE Transactions on Geoscience and Remote Sensing. https://doi.org/10.1109/TGRS.2020.3043335

Tschudi, M. A., Meier, W. N., & Stewart, J. S. (2020). An enhancement to sea ice motion and age products at the National Snow and Ice Data Center (NSIDC). *The Cryosphere*, *14* (5), 1519–1536. https://doi.org/10.5194/tc-14-1519-2020

von Albedyll, L., Haas, C., & Dierking, W. (2021). Linking sea ice deformation to ice thickness redistribution using high-resolution satellite and airborne observations. *The Cryosphere*, *15* (5), 2167–2186. https://doi.org/10.5194/tc-15-2167-2021

von Albedyll, L., Hendricks, S., Hutter, N., Murashkin, D., Kaleschke, L., Willmes, S., Thielke, L., Tian-Kunze, X., Spreen, G., & Haas, C. (2024). Lead fractions from SAR-derived sea ice divergence during MOSAiC. *The Cryosphere*, *18* (3), 1259–1285. https://doi.org/10.5194/tc-18-1259-2024

Wang, Q., Danilov, S., Jung, T., Kaleschke, L., & Wernecke, A. (2016). Sea ice leads in the Arctic Ocean: Model assessment, interannual variability and trends. *Geophysical Research Letters*, *43* (13), 7019–7027. https://doi.org/10.1002/2016GL068696

https://doi.org/10.5194/egusphere-2026-4668
Preprint. Discussion started: 31 August 2026
© Author(s) 2026. CC BY 4.0 License.

Wang, X., Chen, R., Li, C., Chen, Z., Hui, F., & Cheng, X. (2022). An Intercomparison of Satellite Derived Arctic Sea Ice Motion Products. *Remote Sensing*, *14* (5), Article 5. https://doi.org/10.3390/rs14051261

Wang, X., Lu, R., Wang, S.-Y., Chen, R.-T., Chen, Z.-Q., Hui, F.-M., Huang, H.-B., & Cheng, X. (2023). Assessing CMIP6 simulations of Arctic sea ice drift: Role of near-surface wind and surface ocean current in model performance. *Advances in Climate Change Research*, *14* (5), 691–706. https://doi.org/10.1016/j.accre.2023.09.005

Wang, Y., Li, T., Zhao, J., Tang, Y., Wang, X., Zhong, W., & Liu, Y. (2025). A Drift-Towing Ocean Profiling (DTOP) System for Monitoring the Ice-Covered Upper Ocean in Polar Regions. *Journal of Atmospheric and Oceanic Technology*, *42* (12), 1617–1628. https://doi.org/10.1175/JTECH-D-24-0102.1

Woods Hole Oceanographic Institution. (n.d.). *Ice Tethered Profilers*. Ice Tethered Profilers. Retrieved February 9, 2026, from https://www2.whoi.edu/site/itp/

Yang, Y., Xie, T., Sun, C., Wang, C., Li, J., & Zhang, X. (2024). Improvement of Sea Ice Drift Extraction Based on Feature Tracking from C-SAR/01 Imagery. *IEEE Journal of Selected Topics in Applied Earth Observations and Remote Sensing*, *17*, 10237–10251. IEEE Journal of Selected Topics in Applied Earth Observations and Remote Sensing. https://doi.org/10.1109/JSTARS.2024.3403919

Yu, J., Yang, Y., Liu, A. K., & Zhao, Y. (2009). Analysis of sea ice motion and deformation in the marginal ice zone of the Bering Sea using SAR data. *International Journal of Remote Sensing*, *30* (14), 3603–3611. https://doi.org/10.1080/01431160802585355

https://doi.org/10.5194/egusphere-2026-4668
Preprint. Discussion started: 31 August 2026
© Author(s) 2026. CC BY 4.0 License.

Zhang, J., Weijer, W., Steele, M., Cheng, W., Verma, T., & Veneziani, M. (2021). Labrador Sea freshening linked to Beaufort Gyre freshwater release. *Nature Communications*, *12* (1), Article 1. https://doi.org/10.1038/s41467-021-21470-3

Zhang, X., Zhu, Y., Zhang, J., Meng, J., Li, X., & Li, X. (2020). An Algorithm for Sea Ice Drift Retrieval Based on Trend of Ice Drift Constraints from Sentinel-1 SAR Data. *Journal of Coastal Research*, *102* (sp1), 113–126. https://doi.org/10.2112/SI102-015.1

Zhou, L., Xu, S., Liu, J., & Wang, B. (2018). On the retrieval of sea ice thickness and snow depth using concurrent laser altimetry and L-band remote sensing data. *The Cryosphere*, *12* (3), 993–1012. https://doi.org/10.5194/tc-12-993-2018